



# *In situ* construction of Sn-doped structurally compatible heterojunction with enhanced interfacial electric field for photocatalytic pollutants removal and CO<sub>2</sub> reduction

Hanbo Yu<sup>a,b</sup>, Jinhui Huang<sup>a,b,\*</sup>, Longbo Jiang<sup>a,b</sup>, Lijian Leng<sup>c</sup>, Kaixin Yi<sup>a,b</sup>, Wei Zhang<sup>a,b</sup>, Chenyu Zhang<sup>a,b</sup>, Xingzhong Yuan<sup>a,b</sup>

<sup>a</sup> College of Environmental Science and Engineering, Hunan University, Changsha, 410082, China

<sup>b</sup> Laboratory of Environment Biology and Pollution Control, Hunan University, Ministry of Education, Changsha, 410082, China

<sup>c</sup> School of Energy Science and Engineering, Central South University, Changsha, 410083, China

## ARTICLE INFO

### Keywords:

Heterojunction  
Interfacial electric field  
Sn-doped BiOBr  
DFT  
BiOIO<sub>3</sub>

## ABSTRACT

Fabrication of heterojunction photocatalysts is a promising strategy for achieving spatial charge separation, for which the interfacial electric field is the linchpin. However, the current density of interfacial electric field still have room for enhancement. In this study, we first demonstrated the regulation of interfacial electric field between bismuth semiconductors assisted by stannum (Sn) doping, raising the surface charge transfer efficiency from 27.25 % of BiOBr/BiOIO<sub>3</sub> to 38.08 % of Sn-BiOBr/BiOIO<sub>3</sub> composite. Correspondingly, the visible-light induced degradation rates towards tetracycline, 2, 4-chlorophenol and Rhodamine B exhibited 4.2-, 4.7- and 31.5-fold increase, respectively. Meanwhile, the CO<sub>2</sub> photoreduction activity was also improved. The density functional theory calculation results unveiled that the Sn<sup>2+</sup>/Sn<sup>4+</sup> redox couple could cause charge redistribution at interface and a distinctly unidirectional interfacial electric field with the direction from BiOIO<sub>3</sub> to Sn-BiOBr was formed. This study provides a universal strategy for the design of bismuth-containing heterojunction with tunable interfacial electric field.

## 1. Introduction

Photocatalysis for the removal of pollutants and the production of renewable energy source has become an increasingly promising technology to support the sustainable development of human being [1,2]. Therefore, much theoretical and experimental efforts have been devoted to developing new photocatalysts with broad light response range and accessible active sites [3,4]. Upon these materials, further modulations are required for achieving rapid charge separation and sufficient light absorption, for instance, doping, morphology control, noble metal deposition and heterostructure construction. Among them, hybridization of semiconductors is a commonly used strategy to improve photocatalytic activity which provides a potential strategy to tackle the barrier of charge extraction [5–9]. Specifically, the interfacial electric field plays a pivotal role in promoting the photoinduced electrons (e<sup>-</sup>) and holes (h<sup>+</sup>) to migrate along opposite directions, resulting in the fact that positive charges and negative charges accumulate on the two components separately [10–14]. For example, Yao et al. *in situ* grew graphene

on g-C<sub>3</sub>N<sub>4</sub> to achieve a tight barrier-free interface [15]. The formation of spontaneous polarization electric field at interface drove the electrons to transfer from bulk to the redox sites on graphene.

Recently, studies about heterostructures claimed that *in situ* growth of one component on another one with similar crystal architecture could minimize the lattice mismatch at the interface, which improved the structural stability and facilitated the charge transfer between them [16]. Otherwise, the large crystal lattice mismatch could induce the interfacial defects and strain fields because one component would be overly compressed [17]. Considering that most bismuth-based semiconductors share the similar crystal structure, whereby the [Bi<sub>2</sub>O<sub>2</sub>]<sub>2</sub><sup>+</sup> slabs are interlaced with double slabs of anion groups, constructing binary bismuth-containing heterojunction is feasible. To this end, ion exchange approach was widely utilized for the topochemical transformation of bismuth-containing semiconductors with many merits, including low cost, convenient manipulation, morphological homogenization and excellent control over depositing proportion [18]. Using monolayered Bi<sub>2</sub>WO<sub>6</sub> nanosheet as starting material, Xing et al.

\* Corresponding author at: College of Environmental Science and Engineering, Hunan University, Changsha, 410082, China.

E-mail address: [huangjinhui\\_59@163.com](mailto:huangjinhui_59@163.com) (J. Huang).

<https://doi.org/10.1016/j.apcatb.2021.120618>

Received 17 April 2021; Received in revised form 18 July 2021; Accepted 9 August 2021

Available online 12 August 2021

0926-3373/© 2021 Elsevier B.V. All rights reserved.

fabricated a tightly bonded  $\text{Bi}_2\text{WO}_6\text{-Bi}_2\text{O}_2\text{S}$  2D-2D heterojunction with five alternating layers [19]. The strong interfacial bonding dramatically facilitated the charge carrier separation. Chai et al. constructed a  $\text{BiO-I/BiOBr}$  heterojunction films by using  $\text{BiOI}$  as precursor and tetrabutylammonium bromide (TBAB,  $\text{Bu}_4\text{N}^+\text{Br}^-$ ) as bromine source. The  $\text{I}^-$  ions possessed higher nucleophilicity than  $\text{Br}^-$  ions, which tended to react with  $\text{Bu}_4\text{N}^+$ , prompting the partial transformation of  $\text{BiOI}$  to  $\text{BiOBr}$  against solubility product constants. As results, the products were continuous and uniform and the photocatalytic activity was also enhanced. However, monotonous construction of heterojunction can only form an interfacial electric field, in which the charge transfer property is constant. As known, the current photocatalytic performances of binary bismuth-containing heterojunctions are still far from meeting the actual needs. A facile strategy should be developed to further tune the electric field intensity as interface to achieve a more swift charge transfer process.

Incorporation of doping elements into the lattices of a bismuth semiconductor has garnered much attention which can modify the electronic properties and alter the surface affinity for chemical species [20,21]. In comparison to non-metallic elements doping, the substitutions of Bi by metallic elements are deemed more flexible to modulate the optoelectrical and catalytic properties [22]. The redox energy states of metallic dopants mostly lie within the band structure, thereby extending the visible light response and boosting the transfer of  $\text{e}^-$  and  $\text{h}^+$ . However, the influence of doping on the interfacial electric field of heterojunction have long been ignored. Hence, we plan to employ a previously reported  $\text{BiOBr/BiOI}_3$  heterostructure as research model to study the effect of metal doping on the interfacial electric field in depth, as well as optical and physical properties.

Herein, we developed a one-step hydrolysable stannous bromide ( $\text{SnBr}_2$ )-etching method for achieving heterojunction formation and cation doping synchronously. The  $\text{Sn-BiOBr/BiOI}_3$  showed a remarkably improved photocatalytic performance towards organic pollutants degradation and  $\text{CO}_2$  photoreduction. The compounds also possessed good mineralization ability and stability. Various characterization means were conducted to survey and quantify the physicochemical and photoelectrical properties. Furthermore, the electronic structures of different models were analyzed in detail by density-functional-theory (DFT) calculations to look into the influences of Sn-doping on interfacial properties. This method shows a simple and general synthetic applicability to regulate the interfacial electric field between bismuth-containing semiconductors.

## 2. Experimental section

### 2.1. Materials

All starting chemicals ( $\text{Bi}(\text{NO}_3)_3\cdot 5\text{H}_2\text{O}$ ,  $\text{KIO}_3$ ,  $\text{SnBr}_2$ ) used in this work were analytical grade and utilized without any purification processes.

### 2.2. Synthesis of $\text{BiOI}_3$ photocatalyst

In a typical procedure, 1 mmol of  $\text{Bi}(\text{NO}_3)_3\cdot 5\text{H}_2\text{O}$  and 1 mmol of  $\text{KIO}_3$  were dissolved in 70 mL of deionized water under vigorous magnetic stirring for 0.5 h at room temperature. Then the mixed solution was transferred into a 100 mL Teflon-lined stainless autoclave and heated at  $150\text{ }^\circ\text{C}$  for 6 h in an electric heating oven. The obtained white powder was centrifuged, washed alternately with deionized water and absolute ethanol for three times and then dried at  $60\text{ }^\circ\text{C}$  for 6 h.

### 2.3. Synthesis of Sn-doped $\text{BiOBr/BiOI}_3$ photocatalyst

A series of  $\text{Sn-BiOBr/BiOI}_3$  samples were synthesized by partially etching  $\text{BiOI}_3$  by metal bromide. Typically, certain amount of  $\text{SnBr}_2$  was added in a mixture of 20 mL of deionized water and 20 mL of

ethanol under vigorous stirring for 10 min. Then 200 mg of as-prepared  $\text{BiOI}_3$  was slowly added into the above solution and subjected to continuous magnetic stirring for 1.5 h. Finally, the turbid solution was sealed in a Teflon-lined autoclave and heated at  $120\text{ }^\circ\text{C}$  for 6 h. The precipitates with yellow color were centrifuged, washed with deionized water and absolute ethanol for several times and dried at  $60\text{ }^\circ\text{C}$  overnight. The final products ( $\text{Sn-doped BiOBr/BiOI}_3$ ) with 4 mg, 8 mg, 12 mg, 16 mg and 20 mg of  $\text{SnBr}_2$  were denoted as BSB-4, BSB-8, BSB-12, BSB-16 and BSB-20, respectively. The undoped  $\text{BiOBr/BiOI}_3$  was fabricated following the similar procedure unless the 16 mg of  $\text{SnBr}_2$  was replaced by 0.3 mL hydrogen bromide.

### 2.4. Sample characterization

The X-ray diffraction (XRD) patterns were implemented on a Bruker D8 Advance instrument operating with Cu-K $\alpha$  source in a  $2\theta$  range from  $10^\circ$  to  $80^\circ$  to identify the phase structure of as-prepared samples. X-ray photoelectron spectroscopy (XPS) measurements were carried out on an ESCALAB 250Xi spectrometer (Thermo Fisher Scientific, UK). The  $\text{N}_2$  gas adsorption-desorption method was used to measure the specific surface area of samples by the assist of ASAP 2020 instrument (Micromeritics, USA). The nano-/micro-structure morphologies, and elemental information were characterized by the Field Emission Scanning Electron Microscopy (FESEM, Nova NanoSEM 450) and Field Emission Transmission Electron Microscope (FETEM, Tecnai G2 F20), respectively. The UV-vis diffuse reflectance spectra (DRS) were observed by a Varian Cary 300 spectrometer in wavelength range of 200 nm–800 nm and  $\text{BaSO}_4$  as the reference. The steady-state photoluminescence (PL) spectra and ns-level time-resolved PL decay spectra were recorded on a FLS980 Series of Fluorescence Spectrometers with an excitation wavelength of 320 nm. The Shimadzu TOCVCPH analyzer was used to investigate the mineralization ability of photocatalysts. The electron spin resonance (ESR) were determined by a Bruker ER200-SRC spectrometer.

### 2.5. Photocatalytic pollutant degradation

The photocatalytic degradation activity of  $\text{Sn-BiOBr/BiOBr}$  composite was evaluated by using tetracycline hydrochloride (TC) as target pollutant under visible light irradiation. In a typical procedure, 50 mg catalyst was uniformly dispersed into 100 mL of  $20\text{ mg L}^{-1}$  TC solution. The visible-light source was a 300 W Xenon lamp equipped a light filter ( $\lambda > 400\text{ nm}$ ) to cut off UV light. The distance of light source from the reaction device was 13 cm. Prior to irradiation, the mixed solution was kept stirring in dark condition for 60 min to achieve the adsorption-desorption equilibrium. 3 mL aliquot was taken out from the reactor at a given time interval of irradiation and centrifuged for further analysis. The reaction solution was analyzed by UV-vis spectrophotometer at the characteristic optical absorption peak of 277 nm. Moreover, Rhodamine B (RhB, 20 mg/L) and 2, 4-chlorophenol (2, 4-DCP, 10 mg/L) were also employed as additional processing objects to test the applicability of the as-obtained catalysts.

### 2.6. Photocatalytic $\text{CO}_2$ reduction

The photocatalytic  $\text{CO}_2$  reduction capacity was tested in a gas-solid reactor (Scheme S1) and the reduction gas phase product was tested in a Labsolar-6A all glass automatic on-line trace gas analysis system (Beijing, Perfectlight). The visible-light source was a 300 W Xenon lamp (PLS-SXE300D/300DUV) and the DC-0506 low-temperature thermostat bath (Beijing, Perfectlight) was applied to keep the temperature of the reaction cell at  $20\text{ }^\circ\text{C}$ . The watch glass (*ca.*  $27\text{ cm}^2$ ) with 20 mg of uniformly dispersed as-prepared photocatalyst was placed on a glass bracket at the upper layer of a reactor (400 mL). Before the reactor was exhaustively vacuumized, 1.70 g  $\text{NaHCO}_3$  was put into its bottom. 16 mL  $\text{H}_2\text{SO}_4$  (4 M) was injected into the cell to react with  $\text{NaHCO}_3$  for inwardly generating  $\text{CO}_2$  gas at *ca.* 80 kPa. Subsequently, 1 mL of the

resultant gas was automatically withdrawn and qualitatively analyzed by a GC9790II gas chromatograph (Fuli Analytical Instrument Co., Ltd., China) equipped with a TDX - 01 column (FID detector, carrier gas: Ar, column temperature: 80 °C, inlet temperature: 120 °C, and test temperature: 140 °C).

## 2.7. DFT calculation

The structure relaxation, differential charge density, DOS, electronic band structure and single-point energies were investigated by the DFT calculations implemented in the Vienna Ab-initio Simulation Package (VASP) code. The exchange-correlation interactions were described by the generalized gradient approximation (GGA) of Perdew-Burke-Ernzerhof (PBE). The van der Waals interactions were treated using the D2 method proposed by Grimme. The cutoff energy for the plane-wave expansion was set as 500 eV, the Brillouin zone was performed with a  $4 \times 4 \times 2$  Monkhorst Pack grid and the threshold of the self-consistent-

field energy for all atoms were converged to  $10^{-5}$ . All of the computational parameters were set as accurate to ensure the accuracy of present purpose.

## 3. Results and discussion

### 3.1. Compositional and structural information

Previous way to prepare BiOBr/BiO<sub>3</sub> heterostructure was to add extra Bi<sup>3+</sup> and Br<sup>-</sup> into the acetic acid solution containing BiO<sub>3</sub> precursor [23]. Also, it was possible to obtain the BiOBr/BiO<sub>3</sub> heterostructure by etching BiO<sub>3</sub> with hydrobromic acid, where BiO<sup>+</sup> was released and subsequently reacted with Br<sup>-</sup> ions to form BiOBr [24]. However, these methods were unsafe (acetic acid and hydrobromic acid were highly corrosive) and difficult to control (the injection speed of KBr solution or hydrobromic acid should be carefully maintained to make the products uniform). Even worse, BiOBr/BiO<sub>3</sub> hybrid by these

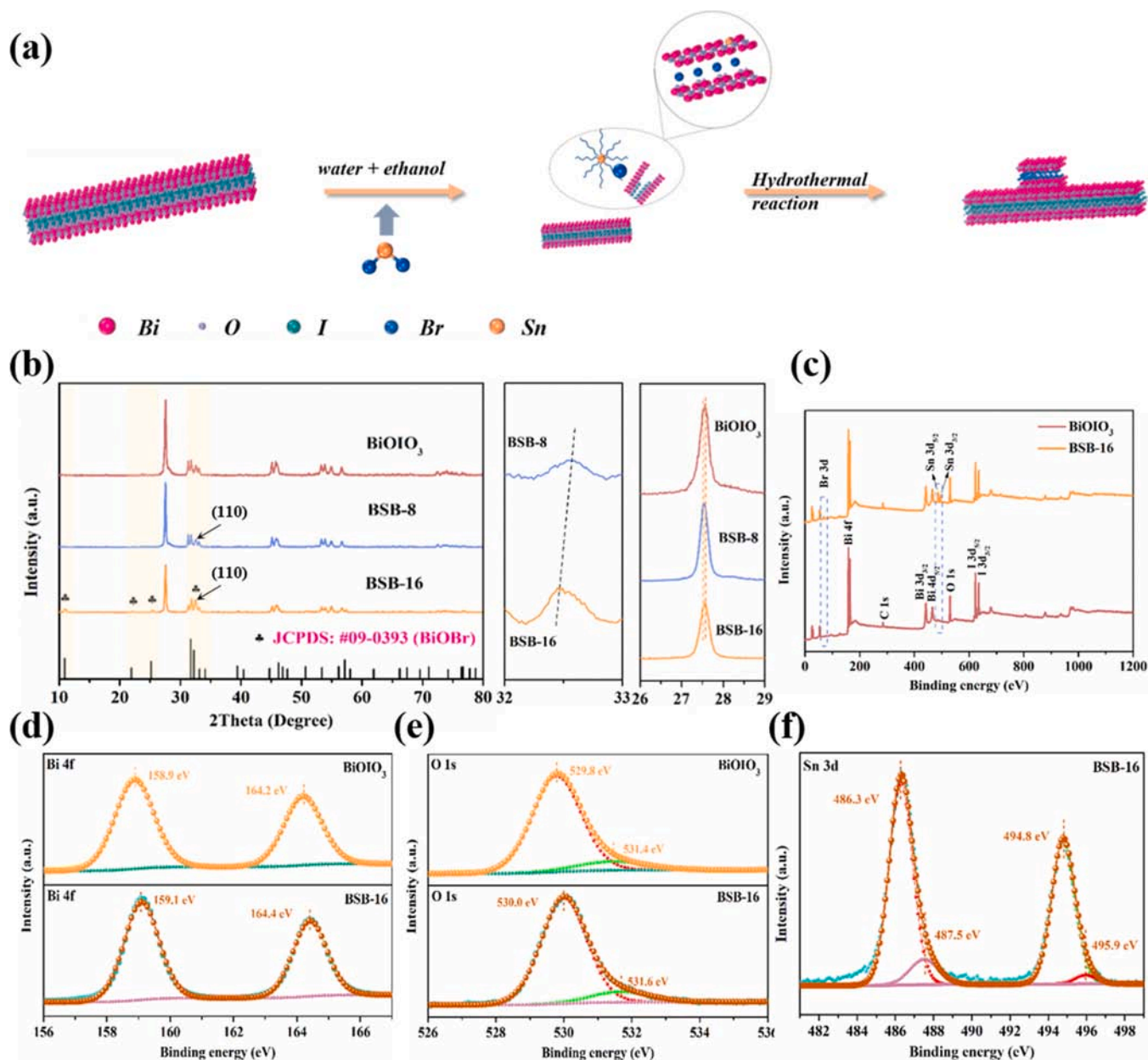


Fig. 1. (a) Schematic illustration for the synthetic process of Sn-BiOBr/BiO<sub>3</sub> (BSB) samples. (b) XRD patterns and (c, d, e and f) XPS of survey, Bi 4f, O 1s and Sn 3d spectra of pure BiO<sub>3</sub> and BSB.

methods suffered from low response of solar light, resulting in the fact that it was only applied to treat photosensitive pollutants (dyes). Given that  $\text{SnBr}_2$  tended to release  $\text{H}^+$  because of the highly hydrolysable nature, it was expected that the acid condition was similar with the case of hydrobromic acid to form heterostructure [25]. Fig. 1a displayed the synthetic process of Sn-BiOBr/ $\text{BiOIO}_3$  heterostructure. Initially,  $\text{BiOIO}_3$  was synthesized using  $\text{KIO}_3$  and  $\text{Bi}(\text{NO}_3)_3 \cdot 5\text{H}_2\text{O}$  as the sources of  $\text{IO}_3$  and Bi, which were inexpensive and environmentally friendly. After adding  $\text{BiOIO}_3$  into the  $\text{SnBr}_2$  mixture solution, the  $\text{BiOIO}_3$  was partially etched accompanying with the release of  $\text{BiO}^+$ . Then the Sn complex and  $\text{Br}^-$  ions produced by proper hydrolysis of  $\text{SnBr}_2$  could bind with  $\text{BiO}^+$  to transform into Sn-doped BiOBr on the surface of  $\text{BiOIO}_3$ .

The formation and crystal structure of the prepared samples were first analyzed by X-ray powder diffraction (XRD) and presented in Fig. 1b. The characteristic diffraction peaks of  $\text{BiOIO}_3$  accorded well with orthorhombic  $\text{BiOIO}_3$ , demonstrating the pure phase [26]. The typical peaks of  $\text{BiOIO}_3$  were maintained intact in the BSB composites, indicating that the addition of  $\text{SnBr}_2$  did not affect the crystal phase of  $\text{BiOIO}_3$ . However, some characteristic diffraction peaks belonging to BiOBr (JCPDS No. 09-0393) appeared and gradually intensified with the increment of  $\text{SnBr}_2$ . No distinct diffraction peaks of other impurities, such as  $\text{Bi}_2\text{Sn}_2\text{O}_7$  or  $\text{SnO}_x$  could be detected, indicating that  $\text{Sn}^{2+}$  cations were topochemically doped into the BiOBr lattice [27]. Moreover, the amplified XRD result showed that the (110) peak of BiOBr in BSB samples shifted to lower degree, which might result from the larger ionic radius of  $\text{Sn}^{2+}$  (1.12 Å) than that of  $\text{Bi}^{3+}$  (1.03 Å) [28]. However, the patterns of undoped BiOBr/ $\text{BiOIO}_3$  exhibited no shift (Fig. S1). This subtle change further demonstrated the Sn atoms had been doped into

the lattice of BiOBr. More importantly, the highest characteristic peak of  $\text{BiOIO}_3$  at  $27.59^\circ$  had no shift after etching, further consolidating that Sn was doped into BiOBr instead of  $\text{BiOIO}_3$ . X-ray photoelectron spectroscopy (XPS) was conducted to reveal the surface states of  $\text{BiOIO}_3$  and BSB, further illuminating the formation of heterojunction and the Sn-doping effect by the metal bromide-involved etching method. The survey spectra of  $\text{BiOIO}_3$  accurately displayed the three component elements of Bi, O and I (Fig. 1c). In comparison to  $\text{BiOIO}_3$ , three obviously new peaks at 68.4 eV, 486.9 eV and 495.3 eV appeared in the survey spectra of BSB respectively, suggesting the generation of Sn-BiOBr constituent. Specifically, the peaks at 158.9 eV and 164.2 eV of  $\text{BiOIO}_3$  (Fig. 1d) corresponded to  $\text{Bi } 4f_{7/2}$  and  $\text{Bi } 4f_{5/2}$  of trivalent bismuth ion ( $\text{Bi}^{3+}$ ), respectively [29]. After treating by  $\text{SnBr}_2$ ,  $\text{Bi}^{3+}$  peaks of BSB shifted slightly to higher binding energy. However, previous report claimed that  $\text{Sn}^{2+}$  had almost no effect on the chemical environment around  $\text{Bi}^{3+}$  [27]. Therefore, this red shift could be attributed to the formation of heterostructure. Similarly, the O 1s peaks (Fig. 1e) divulged the same shifting regularity and two peaks at 68.4 eV and 69.5 eV were appeared in the Br 3d spectrum (Fig. S2), further demonstrating the successful formation of heterojunction. As shown in Fig. 1f, the Sn 3d spectrum of BSB could be divided into four peaks at 486.3 eV, 487.5 eV, 494.8 eV and 495.9 eV respectively, signifying the dominant existence of 2+ states and subordinate existence of 4+ states of Sn. These results also implied the successful formation of heterostructure and implantation of  $\text{Sn}^{2+}/\text{Sn}^{4+}$  redox couple.

To fully determine the effect of in-situ etching method on the present materials, scanning electron microscopy (SEM) and transmission electron microscopy (TEM) were performed to characterize the prepared

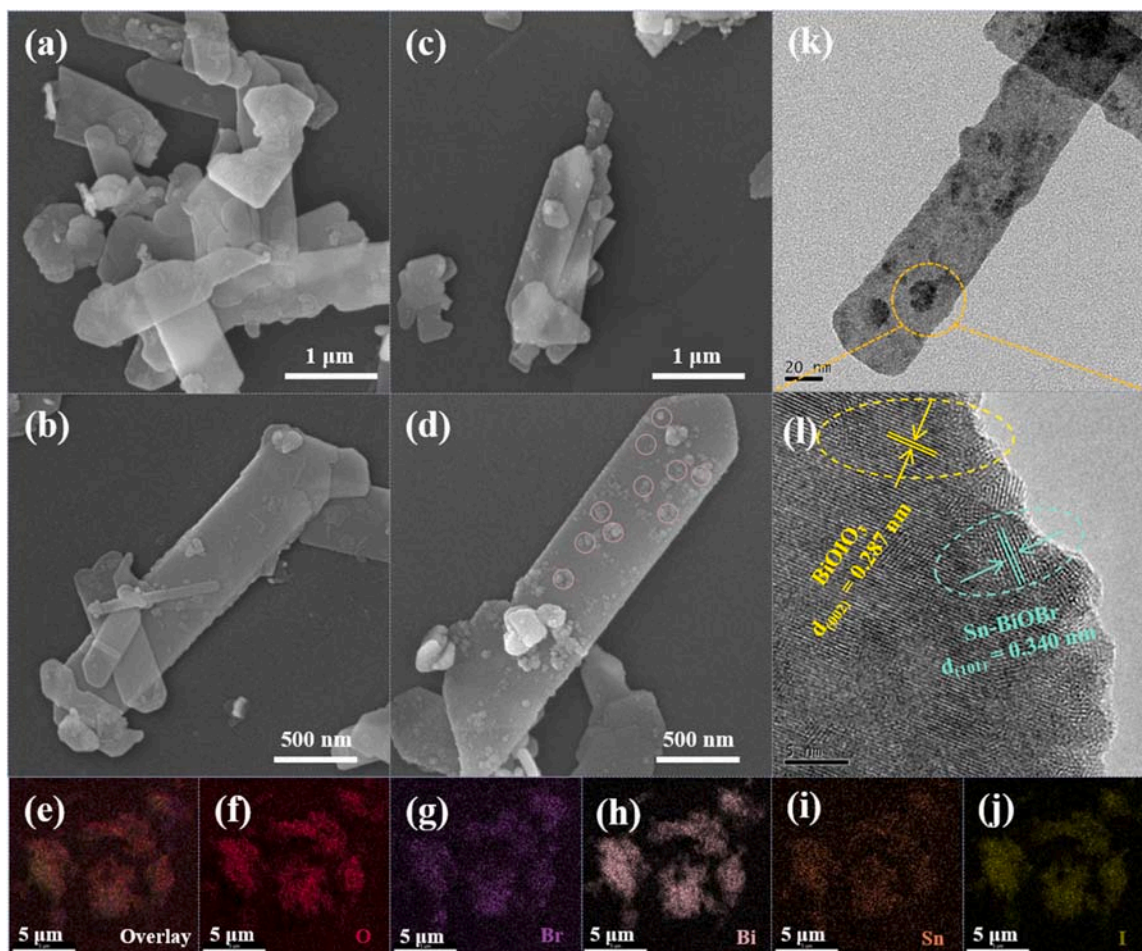


Fig. 2. SEM images of (a and b) pure  $\text{BiOIO}_3$  and (c and d) BSB-16. (e–j) FESEM-EDS elemental mapping of BSB-16. TEM image (k) and HRTEM image (l) of BSB-16.

samples visually. As displayed in Fig. 2a and b, the pristine  $\text{BiOIO}_3$  was composed of nanobelts with smooth surface. The average length was around 1.5  $\mu\text{m}$ . When  $\text{SnBr}_2$  was introduced, no noticeable change was observed for BSB-16 from the SEM images (Fig. 2c). The overall banded structures were preserved. However, the surface of the metal bromide-treated nanobelts became coarse in the magnified SEM image (Fig. 2d), where lots of nanoparticles formed on the nanobelts (marked by light pink circles). This might be because partial  $\text{BiO}^+$  slabs were tailored and further combined with  $\text{Br}^-$  to form  $\text{BiOBr}$ . The similar phenomenon was also observed on undoped  $\text{BiOBr}/\text{BiOIO}_3$  composite (Fig. S3). In order to further authenticate the presence of hybridization, FESEM-EDS elemental mapping was collected. As shown in Fig. 2e–j, the elements of O, Bi, Br, Sn and I distributed across the BSB-16 uniformly and no other foreign elements could be detected. Furthermore, TEM and HRTEM technologies were conducted to investigate the microscopic changes of the as-obtained materials. As shown in Fig. 2k, the  $\text{BiOIO}_3$  nanobelts were almost transparent, demonstrating the existence of ultrathin nanostructure. Some darker particles were observed at some places, which could be ascribed to the newly formed  $\text{Sn-BiOBr}$ . The high-resolution transmission electron microscopy (HRTEM) was conducted

on the top facet to probe the exposed facets and further prove the existence of  $\text{Sn-BiOBr}$ . Well-crystallized single crystalline could be observed for the synthesized  $\text{BiOIO}_3$  catalysts (Fig. S4a). The interplanar spacing of the top facet was 0.287 nm and 0.283 nm, which were assigned to the (002) and (200) lattice planes of orthorhombic  $\text{BiOIO}_3$ , respectively [30]. The FFT patterns (Fig. S4b) displayed the angle between diverse planes. The facet angle in the top facets were determined to be  $45^\circ$ , which was in agreement with the theoretical value of that between the (002) and (101) planes. According to the above results, the top and bottom surfaces of the as-prepared  $\text{BiOIO}_3$  nanobelts were identified as (010) facets. With respect to the  $\text{Sn-BiOBr}/\text{BiOIO}_3$  heterojunction as shown in Fig. 2l, two different lattice fringes, corresponding to the (002) plane (0.287 nm) of  $\text{BiOIO}_3$  and (101) plane (0.340 nm) of  $\text{Sn-doped BiOBr}$  were observed. Compared with the (101) lattice (0.347 nm) of pure  $\text{BiOBr}$ , the lattice spacing of  $\text{Sn-doped BiOBr}$  was marginally smaller, which was in good agreement with the blue-shifted XRD patterns [31]. Apparently, the characteristics of both  $\text{BiOIO}_3$  and  $\text{Sn-BiOBr}$  existed in visual field, demonstrating the successful combination of the materials.

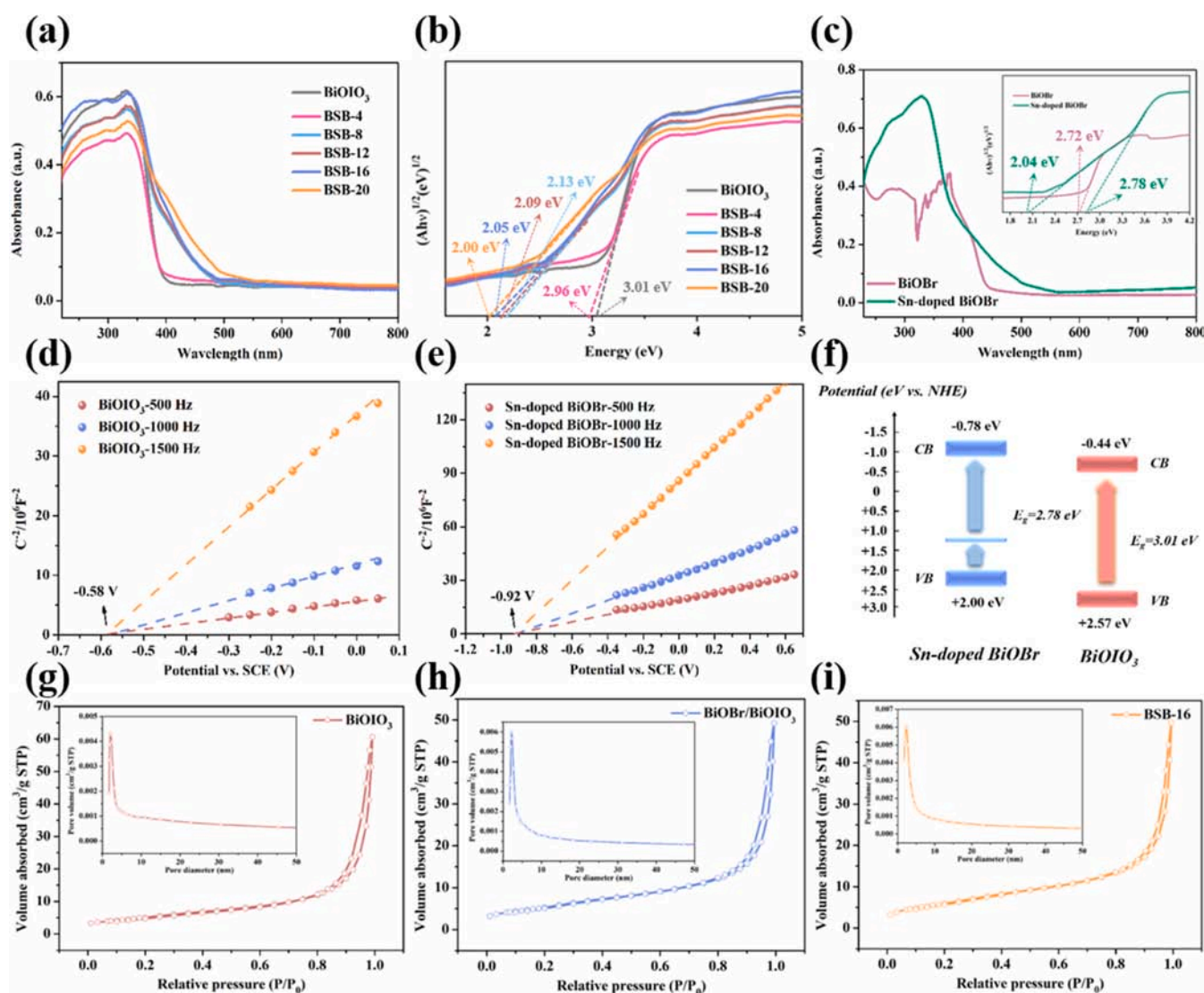


Fig. 3. (a) UV-vis DRS and (b) corresponding plots of transformed Kubelka-Munk function for  $\text{BiOIO}_3$  and BSB-x samples. (c) Comparison of optical absorption property between pure  $\text{BiOBr}$  and Sn-doped  $\text{BiOBr}$ ; the inset is plots of transformed Kubelka-Munk function for Sn-doped  $\text{BiOBr}$ . Mott-Schottky plots of (d) pure  $\text{BiOIO}_3$  and (e) Sn-doped  $\text{BiOBr}$ . (f) The schematic illustration for the band structures of pure  $\text{BiOIO}_3$  and Sn-doped  $\text{BiOBr}$ . Nitrogen adsorption-desorption isotherms for (g)  $\text{BiOIO}_3$ , (h)  $\text{BiOBr}/\text{BiOIO}_3$  and (i) BSB-16 and corresponding pore size distribution.

### 3.2. Optical and physical properties

To further investigate the optical absorption properties and band structure of the prepared BiOIO<sub>3</sub> and BSB-x samples, the UV–vis diffuse reflectance spectroscopy (DRS) and Mott-schottky plots were measured. As shown in Fig. 3a, the absorption edge of pure BiOIO<sub>3</sub> situated at ca. 400 nm. With in-situ etching by SnBr<sub>2</sub>, the absorption edge exhibited significant redshift, and the photoabsorption range was gradually extended to 500 nm from BSB-4 to BSB-20. Further, the corresponding band gap energies of samples were calculated by the transformed Kubelka-Munk function [32] and shown in Fig. 3b. The band gap was determined as 3.01 eV for pure BiOIO<sub>3</sub>. With the increase of SnBr<sub>2</sub>, the band gaps of BSB-x narrowed from 2.96 to 2.00 eV, corresponding to the extended optical absorption ranges. In order to ascertain the contribution of Sn doping to the improved visible light absorption ability, a comparison of DRS spectra between pure BiOBr and Sn-doped BiOBr were conducted as shown in Fig. 3c. The absorption edge of BiOBr was located at around 450 nm, while that of Sn-doped BiOBr was about 420 nm. However, Sn-doped BiOBr showed an absorption tail which could receive light up to 560 nm. Thus, the Sn-doped BiOBr acted as a photosensitizer to widely extend the light absorption ranges of BSB-x heterojunctions. Meanwhile, the band gap of Sn-doped BiOBr was estimated to be 2.78 eV, which was slightly larger than that of pure BiOBr [33]. Nevertheless, another band gap with much smaller value also existed, which could be attributed to the Sn doping. In fact, the same phenomenon had also occurred on Sn-doped TiO<sub>2</sub> [34]. The Sn<sup>2+</sup>-doping tended to reduce the band gap, while the Sn<sup>4+</sup> would increase the band gap [35]. Therefore, two band gap value appeared in our research. Next, Mott-Schottky analysis in Fig. 3d and e, were employed to investigate the flat-band potentials (E<sub>fb</sub>) of BiOIO<sub>3</sub> and Sn-doped BiOBr, which were −0.58 V and −0.92 V vs. SCE, respectively. All Mott-Schottky plots of BiOIO<sub>3</sub> and Sn-doped BiOBr under different frequencies displayed positive slope linear region, illustrating the n-type nature of samples [36]. Considering the typical difference between the E<sub>fb</sub> potential and conduction band (CB) minimum of an n-type semiconductor was 0–0.2 V, the CB of BiOIO<sub>3</sub> and Sn-doped BiOBr were determined to be −0.44 eV and −0.78 eV vs. NHE, respectively. Based on the above results, the valence band (VB) maximum of BiOIO<sub>3</sub> and Sn-doped BiOBr were +2.57 eV and +2.00 eV calculated by using the empirical formula E<sub>VB</sub> = E<sub>CB</sub> + E<sub>g</sub> (Fig. 3f) [37]. Considering that the Brunauer–Emmett–Teller (BET) surface area of photocatalyst was directly associated with the photocatalytic performance, the nitrogen adsorption-desorption isotherm analysis was employed to determine the specific surface area of different samples. As shown in Fig. 3g–i, the three isotherm curves all displayed type IV feature, and the specific surface area of pure BiOIO<sub>3</sub>, undoped BiOBr/BiOIO<sub>3</sub> and BSB-16 were determined to be 19.05, 20.18 and 22.50 m<sup>2</sup>/g, respectively. The H3 typical hysteresis loop demonstrated that the pore size distribution of these samples located in the mesoporous region. Specifically, the total pore volume of BSB-16 (0.077 cm<sup>3</sup>/g) was slightly smaller than that of pristine BiOIO<sub>3</sub> (0.094 cm<sup>3</sup>/g), which was probably because the in-situ generated Sn-doped BiOBr with pore volume of 0.076 cm<sup>3</sup>/g overlay partial surface of BiOIO<sub>3</sub> (Table S3). This result further verified the afore-mentioned growth pattern that BiO<sup>+</sup> fragments first fell out of BiOIO<sub>3</sub> crystal array and then reassembled with Br<sup>−</sup> and Sn<sup>x+</sup> (x = 2/4) on the BiOIO<sub>3</sub> crystals. Similarly, the average pore diameter of BSB-16 (7.08 nm) was also decreased compared with BiOIO<sub>3</sub> (10.98 nm) and BiOBr/BiOIO<sub>3</sub> (8.16 nm). Generally speaking, relatively larger specific surface area and pore volume could provide more reaction sites, thereby the results of nitrogen adsorption-desorption isotherm analysis seemed to index that the formation of Sn-BiOBr/BiOIO<sub>3</sub> heterojunction was not conducive to the surface reaction.

### 3.3. Influence of Sn-doping on BiOBr

DFT calculations were thus performed to investigate the

photogenerated charge migration mechanism and help us understand the contribution of Sn-doping to the electronic structure of BiOBr. As shown in Fig. 4a<sub>1</sub>, BiOBr was an indirect semiconductor, where conduction band minimum (CBM) was at the G point and the valence band maximum (VBM) was at the G-M connection. The corresponding PDOS for orbitals (Figs. 4a<sub>2</sub> and S5a) showed that the VB of pristine BiOBr was mainly composed of Br p-orbitals with major hybridization with O p-orbitals and Bi s-orbitals, while the CB was contributed by the p-orbitals of Bi. Upon the substitution of stannum for lattice bismuth atoms in BiOBr (Fig. 4b<sub>1</sub>), the band gap was slightly enlarged, in consistence with the experimental phenomenon (Fig. 3c). However, a new impurity band appeared in Sn-BiOBr, which was mainly composed of Sn s-orbitals, Sn p-orbitals, O p-orbitals and Br p-orbitals (Figs. 4b<sub>2</sub> and S6a). This new defect level divided the band gap into two parts, hence giving the possibility for inhibiting the recombination of photogenerated electrons (e<sup>−</sup>) and holes (h<sup>+</sup>) in the bulk. For further understanding the role of Sn-doping in BiOBr, the charge difference between Sn-BiOBr and BiOBr were theoretically determined. It was worth noting that the charge accumulation of O atoms near the Sn was greatly enhanced and the nearest-neighbor Br atom exhibited obvious electron delocalization, indicating that more effective charge transfer occurred, that was, the built-in electric field within BiOBr was enhanced (Fig. 4d). Notably, the Sn dopant was prone to lose electrons after substituting Bi atom, thereby generating oxidation state Sn<sup>4+</sup>. This was coincided well with the experimental result of XPS. To further understand the relationships between doped Sn and the changed band structure, 2 × 2 BiOBr models with or without Sn doping were established to calculate the 3D visualization of highest occupied molecular orbital (HOMO) and the lowest unoccupied molecular orbital (LUMO). As shown in Figs. S5 and S6, the introduction of Sn would only pose impacts on the direction of charge density distributions as the relative atoms of HOMO and LUMO, rather than the charge intensity. In addition, the composition of impurity band (doping level) was visually verified to be stannum atom and its nearby bromine atoms and the nearest four oxygen atoms, where Sn-doping caused obvious localized charge densities around them. These results revealed that the introduction of Sn could rearrange the band structure and promote charge separation. The band gap and density of states of pure BiOIO<sub>3</sub> was also surveyed as displayed in Figs. 4c<sub>1</sub>–c<sub>2</sub> and S7. BiOIO<sub>3</sub> was also an indirect semiconductor. The VB had strong O p-orbital contributions, and the CB was contributed by the involvement of Bi p-states and I p-states slightly hybridized with O p-states.

### 3.4. Photocatalytic performances for pollutants removal and CO<sub>2</sub> reduction

To further assess the influence of SnBr<sub>2</sub>-etching on the photocatalytic activity, TC was selected as the treatment object to investigate the degradation curve under visible light condition. As exhibited in Fig. S8, the photocatalytic degradation of TC was monitored by the variation of UV–vis absorption spectra of TC solution. Obviously, the intensity of characteristic absorption peak (357 nm) decreased with time. The degradation curves and corresponding reaction kinetic values were displayed in Fig. 5a and d. The degradation efficiencies of BSB-x were significantly better than that of pure BiOIO<sub>3</sub> sample under visible light irradiation. Pure BiOIO<sub>3</sub> did not show remarkable degradation performance towards TC removal (32.79 %). However, with an increasing amount of SnBr<sub>2</sub>, the photocatalytic degradation activity of BSB presented an increasing trend due to the simultaneous formation of heterojunction and ion doping. The highest photocatalytic degradation efficiency of TC (85.66 %) was achieved on BSB-16. Nevertheless, when the amount of SnBr<sub>2</sub> exceeded 16 mg, the photocatalytic activity of BSB increased insignificantly because the excessive SnBr<sub>2</sub> might destruct the integrity of BiOIO<sub>3</sub> crystal, thereby provide new recombination sites for photogenerated e<sup>−</sup> and h<sup>+</sup> [38]. The reaction rate constant (k) for the degradation of TC was obtained by the equation that Ln(C/C<sub>0</sub>) = -kt. Evidently, the BSB-16 possessed the highest reaction rate constant of

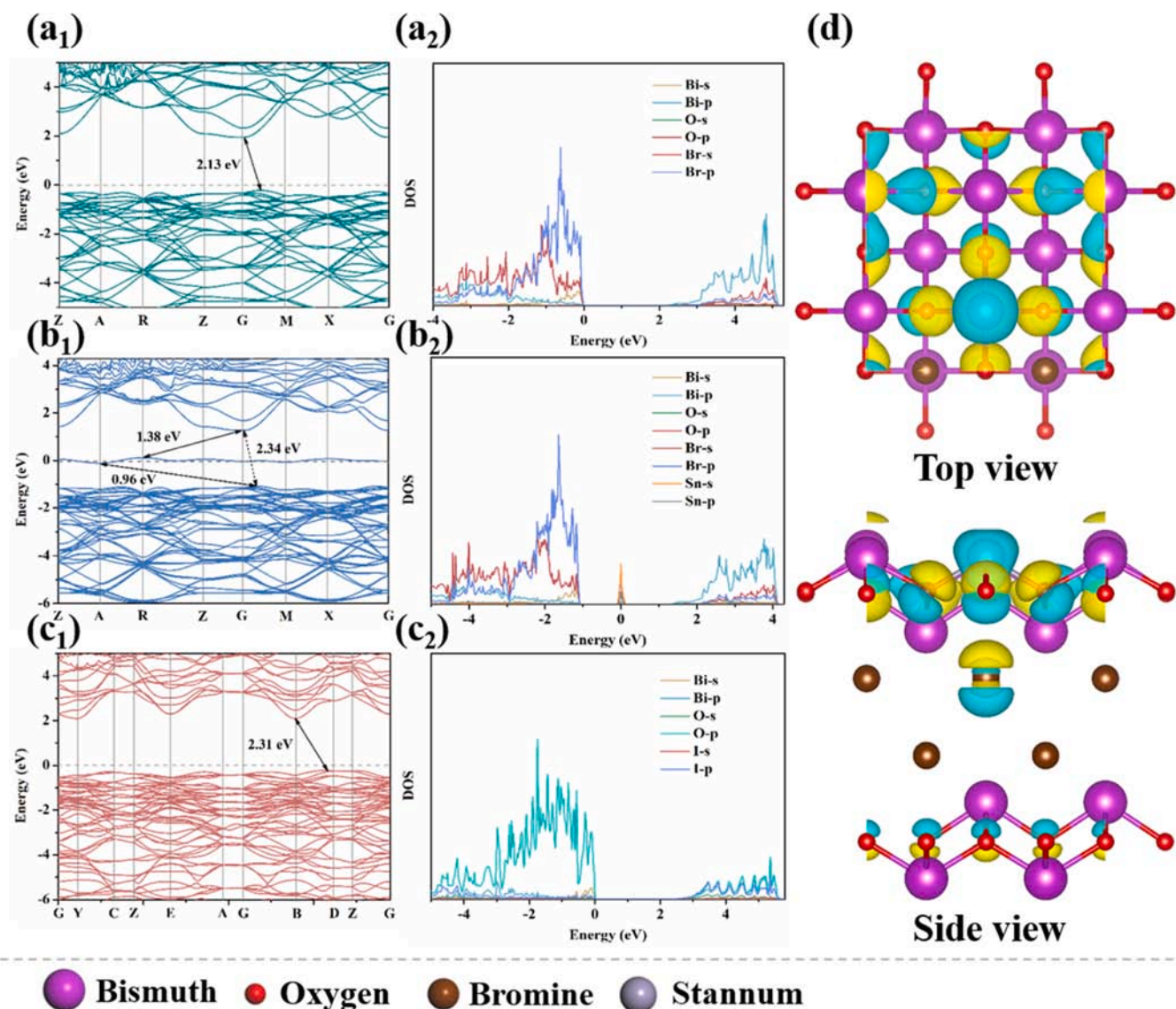
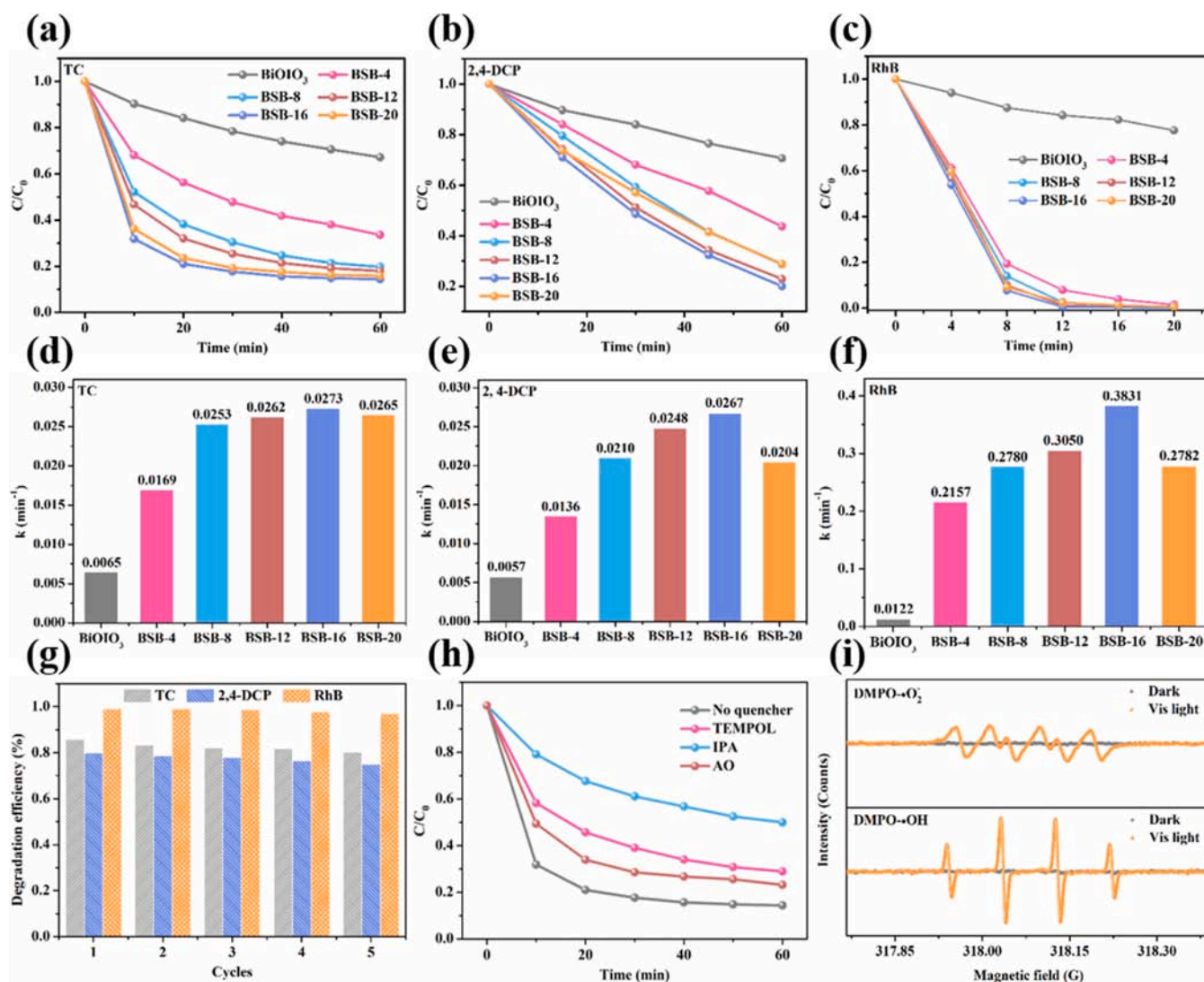


Fig. 4. The band structure of (a<sub>1</sub>) pure BiOBr, (b<sub>1</sub>) Sn-BiOBr and (c<sub>1</sub>) BiOIO<sub>3</sub> and (a<sub>2</sub>, b<sub>2</sub> and c<sub>2</sub>) the corresponding partial density of states (PDOS) for orbitals. (d) 3D charge density difference (0.0076 e/bohr<sup>3</sup>) for Sn-BiOBr (the yellow and blue colors denote the electron accumulation and depletion, respectively) (For interpretation of the references to colour in this figure legend, the reader is referred to the web version of this article).

0.0273 min<sup>-1</sup>, which was about 4.2 times that of pure BiOIO<sub>3</sub>. To further demonstrate the excellent photocatalytic degradation performance of Sn-doped BiOBr/BiOIO<sub>3</sub>, the removal abilities of 2, 4-DCP and RhB were also used as important indicators of photocatalytic performance. As shown in Fig. 5b and c, Sn-doped BiOBr/BiOIO<sub>3</sub> samples showed much improved degradation effects and the BSB-16 was still the best performer with degradation efficiencies of 80.01 % and 99.90 % towards 2, 4-DCP and RhB, respectively. The reaction kinetic rates of 2, 4-DCP and RhB were 0.0267 min<sup>-1</sup> and 0.3831 min<sup>-1</sup>, which were almost 4.7 times and 31.5 times that of pure BiOIO<sub>3</sub>, respectively (Figs. 5e and f, S9 and S10). Control experiments implied that BSB-16 photocatalyst could reach adsorption equilibrium within half an hour (Fig. S11), demonstrating that the dark reaction for 30 min could remove the impact of adsorption on the degradation performance in the degradation experiments. Meanwhile, the natural photolysis of pollutants was negligible under visible light, indicating that these pollutants were degraded by the photocatalysts. Contrastively, undoped BiOBr/BiOIO<sub>3</sub> and Sn-doped BiOBr showed lower performances than the Sn-BiOBr/BiOIO<sub>3</sub> sample (Fig. S12). The results satisfactorily indicated that the Sn-doped BiOBr/BiOIO<sub>3</sub> heterojunctions are widely applicable in the

degradation of various kinds of organic pollutants, such as antibiotics, chlorophenol compounds and dyes, or even many other persistent organic pollutants. To study the mineralization ability of BSB-16 sample, the TOC removal efficiencies were measured and shown in Fig. S13. The removal efficiency of TOC in TC, 2, 4-DCP and RhB aqueous solution were 34.61 %, 56.50 % and 57.73 % with 60 min of visible light irradiation, respectively, further demonstrating the efficacious photocatalytic activity of BSB-16 for organic pollutants degradation. The stability of the BSB-16 was evaluated through cyclic photocatalytic degradation tests. In the five turns of recycle experiments as displayed in Fig. 5g, the BSB-16 still exhibited high degradation activities without noticeable decrease. Moreover, the XRD patterns (Fig. S14) and SEM image (Fig. S15) also verified well-preserved crystalline structure of the BSB-16 after the photocatalytic reaction.

To preliminarily identify the main active species generated in the BSB-16 under visible light irradiation, the trapping experiments were conducted with 4-Hydroxy-2,2,6,6-tetramethyl-1-piperidinyloxy (TEMPO), isopropanol (IPA) and ammonium oxalate (AO) as the quenchers for  $\cdot\text{O}_2^-$ ,  $\cdot\text{OH}$  and  $\text{h}^+$ , respectively. According to Fig. 5h, the degradation efficiency of TC remarkably declined by 35.68 % after adding IPA,



**Fig. 5.** (a–c) Photocatalytic degradation curves of TC, 2, 4-DCP and RhB over the as-obtained samples under visible light irradiation and (d–f) the corresponding reaction dynamic data. (g) Cycling tests for the photocatalytic degradation of different pollutants under visible light irradiation. (h) TC degradation curves over BSB-16 alone and with different quenchers under visible light illumination. (i) ESR signals for DMPO·O<sub>2</sub><sup>-</sup> and DMPO·OH over BSB-16 sample.

indicating the importance of ·OH in the degradation process. The degradation efficiency of TC slightly declined to 71.06 % in the presence of superoxide radical scavengers (TEMPOL). Similarly, the addition of AO also had some negative effect for the TC degradation. The experimental phenomenon manifested that the main reactive species in the reaction system was ·OH and ·O<sub>2</sub><sup>-</sup> and h<sup>+</sup> played secondary roles. To qualitatively test the existence of reactive species, the electron spin resonance (ESR) spin-trap technology based on BSB-16 was performed shown in Fig. 5i. It could be seen that the strong characteristic signals of DMPO·OH were detected, indicating the large amounts of ·OH. Meanwhile, at the same illumination time (10 min), the peak intensity of DMPO·O<sub>2</sub><sup>-</sup> was much weaker than DMPO·OH, proving that just a small amount of ·O<sub>2</sub><sup>-</sup> existed in the reaction system. This result further suggested that the ·OH was the predominant reactive radical during the degradation process, and the ·O<sub>2</sub><sup>-</sup> species only played a minor role.

To evaluate the wide applicability of the as-prepared photocatalyst, the photocatalytic CO<sub>2</sub> reduction activities for the as-prepared samples were also carried out under simulated solar irradiation in a gas–solid reaction setup without any sacrificial agents and cocatalysts. The previous results confirmed that the reductive product in aneroid gas–solid reaction condition was dominantly CO, with no or trace amount of CH<sub>4</sub> or liquid products was detected [39,40]. This could be rationalized

as the relatively effortless occurrence of the two-electron reduction pathway, which was more facile in reaction kinetics than the multi-electron reduction process, such as CH<sub>3</sub>OH production with six-electron or CH<sub>4</sub> production with eight-electron [41,42]. As shown in Fig. 6a, the pure BiOI<sub>3</sub> showed unsatisfactory activity in CO<sub>2</sub> reduction with a CO production of only 8.35 μmol g<sup>-1</sup> within 4 h, mainly owing to its faint light absorption as well as the drastic recombination of photoinduced e<sup>-</sup>-h<sup>+</sup> pairs. In contrast to the BiOI<sub>3</sub>, BSB-16 catalyst exhibited superior CO<sub>2</sub> reduction performance, and the CO production reached 29.58 μmol g<sup>-1</sup>. Fig. 6b displayed the corresponding CO generation rates of these samples. The CO production rate of BSB-16 was 7.40 μmol g<sup>-1</sup> h<sup>-1</sup>, which was 3.54 times higher than that of BiOI<sub>3</sub> (2.09 μmol g<sup>-1</sup> h<sup>-1</sup>). Controlled experiments demonstrated that there was no CO detected under the darkness or without photocatalyst, as well as under simulated solar irradiation by passing over Ar instead of CO<sub>2</sub> in the reaction cell (Fig. 6c). The isotope tracing experiment (Fig. S16) displayed that both <sup>13</sup>CO<sub>2</sub> (*m/z* = 45.1) and <sup>13</sup>CO (*m/z* = 29.1) signals could be detected [43]. These results demonstrated that the evolved CO exclusively originated from the photocatalytic CO<sub>2</sub> reduction process. For the sake of investigating the stability of Sn-doped BiOBr/BiOI<sub>3</sub> in the process of CO<sub>2</sub> reduction experiment, we collected the used BSB-16 and recycled for three successive runs under the same conditions

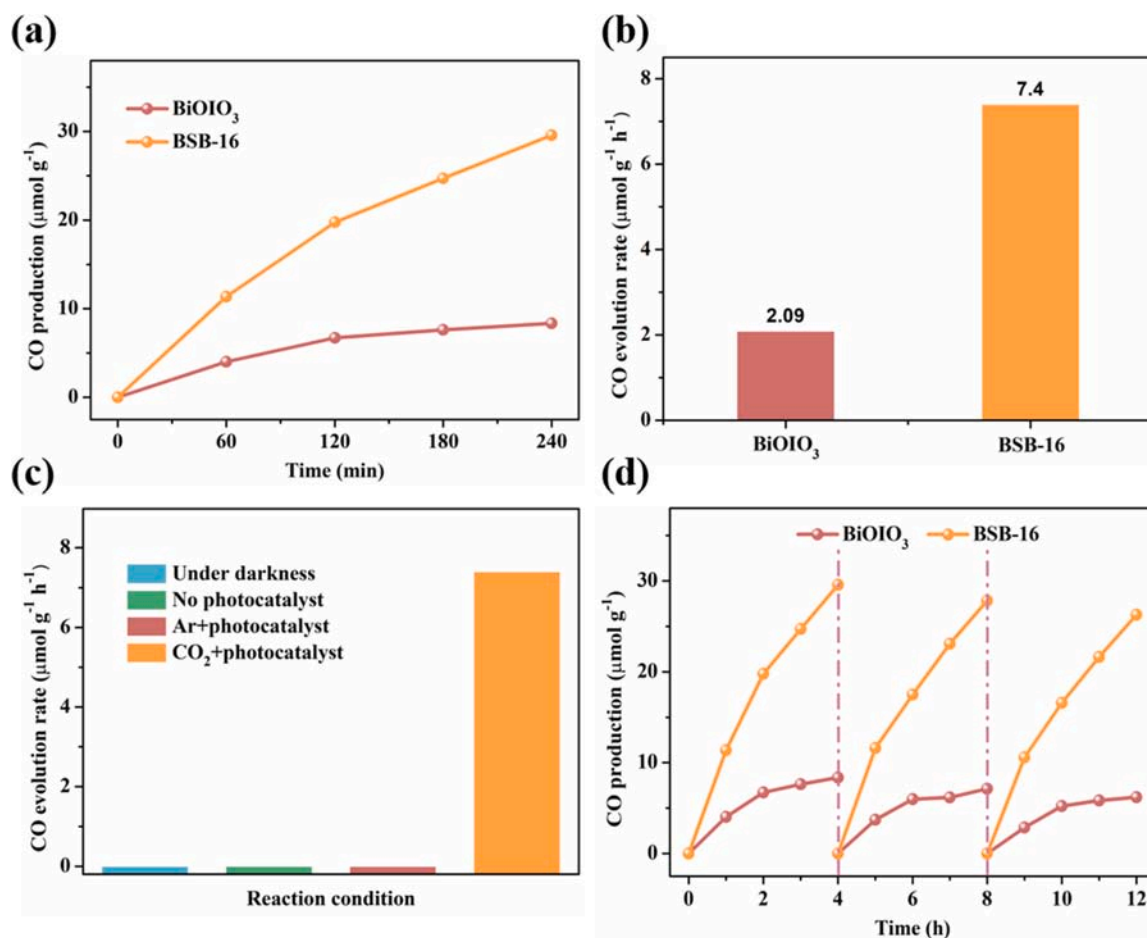


Fig. 6. (a) Time dependence and (b) apparent rate constants for CO evolution by the photoreduction of CO<sub>2</sub> over BiOBr and BSB-16 under simulated sunlight. (c) Control experiments under different conditions. (d) Cycling curves for CO production over BiOBr and BSB-16 samples.

(Fig. 6d). It could be observed a slight reduction in CO production, indicating the high stability of the as-obtained photocatalysts. Overall, the aforementioned results highlighted the high activity and durability of Sn-BiOBr/BiOI<sub>3</sub> composites in photocatalytic applications.

### 3.5. Influence of Sn-doping on the interfacial charge transfer

It is necessary to ask a question. Is the improved photocatalytic activity only relevant to the photosensitization from Sn-doping? Therefore, a series of photoelectrochemistry studies were conducted to survey the microscopic charge transfer behaviors. Firstly, the room temperature photoluminescence (PL) spectroscopy measurement of BiOBr/BiOI<sub>3</sub> and BSB-16 was performed under an excitation wavelength of 340 nm and shown in Fig. 7a, where the BSB-16 exhibited relatively weaker emission intensity owing to its low recombination rate of photogenerated charges. Moreover, the time-resolved fluorescence decay spectroscopy (Fig. 7b) was recorded to further investigate the photoexcited charge carrier transfer dynamics of BiOBr/BiOI<sub>3</sub> and BSB-16, where both of the short and long lifetimes of BSB-16 were considerably prolonged in comparison with those of pristine BiOI<sub>3</sub>. The average lifetime increased from 4.43 ns (BiOBr/BiOI<sub>3</sub>) to 6.79 ns (BSB-16), implying the efficaciously depressed recombination of photogenerated electrons and holes in Sn-doped BiOBr/BiOI<sub>3</sub> heterojunction. Furthermore, the transient photocurrent response test and electrochemical impedance spectroscopy (EIS) also proved this conclusion. As shown in Fig. 7c, the current was generated immediately with the light on, indicating the high photo-sensitivity and valid generation of photoexcitons. Compared to BiOI<sub>3</sub> and BiOBr/BiOI<sub>3</sub>, the BSB-16 sample

showed elevated photocurrent response, confirming that increased free charges had potential to participate photocatalytic reaction under visible light irradiation. Meanwhile, the photocurrent measurement under simulated sunlight irradiation was also implemented as shown in Fig. S17. The photocurrent density of BSB-16 was still the strongest and was approximately 9.2 times higher than that of pure BiOI<sub>3</sub>. This observation clearly stated that the enormously intensified activity was not only associated with photoabsorption. As displayed in Fig. S18a, the decreased diameter on the EIS Nyquist plots of BSB-16 reflected its enhanced interfacial charge mobility, which was beneficial for achieving efficient photocatalytic performance. Based on the above studies, there was no doubt that the recombination of photogenerated electrons and holes could be prevented by constructing Sn-doped BiOBr/BiOI<sub>3</sub> heterojunction.

For the purpose of exploring the specific dynamics of photogenerated charge carriers, a string of measurable electrochemical index were considered to assess how the in-situ construction of Sn-doped BiOBr/BiOI<sub>3</sub> heterojunction assisted with the reduced photoexciton recombination. To start with, the surface charge transfer efficiency ( $\eta_s$ ) was approximated by the photocurrent of BiOBr/BiOI<sub>3</sub> and BSB-16 under visible light irradiation through adding H<sub>2</sub>O<sub>2</sub> into 0.2 M of Na<sub>2</sub>SO<sub>4</sub> electrolyte as a fast electrons scavenger [44]. Typically, the photocurrent density could be defined by the undermentioned equation:

$$J_{H_2O} = J_{max} \times \eta_{sep} \times \eta_{trans} \quad (1)$$

where  $J_{H_2O}$  was the measured photocurrent density,  $J_{max}$  was the theoretical maximum photocurrent density stimulated by the absorbed photo-energy,  $\eta_{sep}$  was the charge separation efficiency within the bulk,

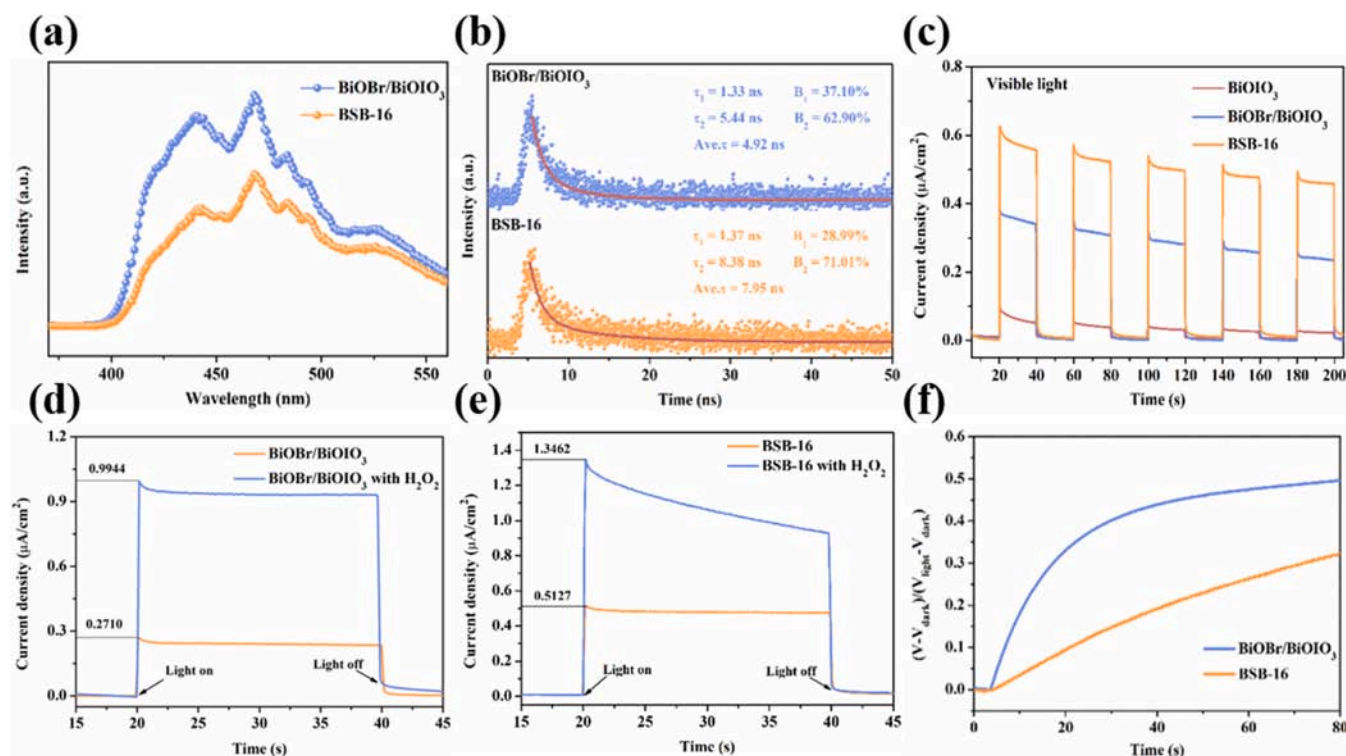


Fig. 7. (a) Photoluminescence spectra under the 340 nm excitation and (b) Fluorescence emission decay spectra of BiOBr/BiOIO<sub>3</sub> and BSB-16. (c) Transient photocurrent response curves of pure BiOBr, BiOBr/BiOIO<sub>3</sub> and BSB-16 under visible light irradiation. Photocurrent density of (d) BiOBr/BiOIO<sub>3</sub> and (e) BSB-16 under visible light irradiation with and without H<sub>2</sub>O<sub>2</sub>. (f) Normalized OCP decay curves of pristine BiOBr/BiOIO<sub>3</sub> and BSB-16.

and  $\eta_{trans}$  was the surface charge transfer efficiency. With H<sub>2</sub>O<sub>2</sub> addition, the surface charge transfer efficiency became greatly increased and the  $\eta_{trans}$  approximately reaches 100%. Consequently, the photocurrent density in the present of H<sub>2</sub>O<sub>2</sub> ( $J_{H_2O_2}$ ) could be expressed as the following equation:

$$J_{H_2O_2} = J_{max} \times \eta_{sep} \quad (2)$$

Herein,  $J_{max}$  and  $\eta_{sep}$  were unchanged in both  $J_{H_2O}$  and  $J_{H_2O_2}$  system because they were the intrinsic properties of each samples. Thus, the surface charge transfer efficiency ( $\eta_{trans}$ ) could be calculated as following equation:

$$\eta_{trans} = J_{H_2O} / J_{H_2O_2} \quad (3)$$

As shown in Fig. 7d and e, the photocurrent densities of BiOBr/BiOIO<sub>3</sub> and BSB-16 rose from 0.2710 and 0.5127  $\mu\text{A}/\text{cm}^2$  to 0.9944 and 1.3462  $\mu\text{A}/\text{cm}^2$ , respectively, after adding H<sub>2</sub>O<sub>2</sub> into electrolyte solution. Accordingly, the surface charge transfer efficiencies of BiOBr/BiOIO<sub>3</sub> and BSB-16 were calculated to be 27.25% and 38.08%, respectively, revealing that BSB-16 held much higher surface charge transfer efficiency in comparison with pristine BiOIO<sub>3</sub>. Furthermore, the surface recombination rates of BiOBr/BiOIO<sub>3</sub> and BSB-16 determined by the normalized decay profile of open-circuit potential (OCP) transients was shown in Fig. 7f [45]. Upon illumination, electrons will be located in CB to be free electrons. Upon light interruption, some electrons will recombine with the trapped holes and adsorbed species on the surface of photocatalysts, named as trapped electrons [46]. According to Bisquert and Vkhrenko, free and trapped electrons always maintain a common equilibrium, thus, the kinetic constants for electron recombination should be first order in electron concentration, which depends on the (surface) structure of the material [47]. Macroscopically, the free electrons drives open circuit potential ( $V_t$ ) to shift toward more negative values. Due to the decrease of the concentration of free electrons after light off, the  $V_t$  will decay slowly and the decay will follow the

pseudo-first order model [48]. The average recombination constant could be estimated by fitting the data with a first-order kinetic model:

$$(V_t - V_{dark}) / (V_{light} - V_{dark}) = 1 - e^{-kt} \quad (3)$$

where  $V_t$ ,  $V_{light}$  and  $V_{dark}$  were OCP at any time ( $t$ ), the photo-stationary OCP value and the dark-stationary OCP value, respectively, and  $k$  represented the pseudo-first order recombination constant ( $\text{s}^{-1}$ ). Distinctly, the OCP decay was markedly impeded after in-situ etching treatment because the spatial separation of charge accumulation centers prompted the photoinduced  $e^-$  and  $h^+$  to survive longer. The fitted recombination rate constant of BSB-16 was determined to be 0.0047  $\text{s}^{-1}$ , which was lowered by ca. 46.9% compared with BiOBr/BiOIO<sub>3</sub> (0.0101  $\text{s}^{-1}$ ). The results of this experiment confirmed that the interfacial recombination was significantly retarded. Beyond surface charge transfer efficiency and recombination rate constant, the lifetime of injected electrons, which was highly correlated with the frequency ( $f$ ) in Bode-phase spectra could also be quantitatively estimated [49]. As depicted in Fig. S18b, the blue shift of the characteristic frequency peak revealed a more rapid electron transport process. According to the equation  $\tau_{inj} = 1/(2\pi f)$ , the approximate lifetime ( $\tau_{inj}$ ) of injected electrons in BSB-16 (34.69  $\mu\text{s}$ ) was estimated to be about 3.9 times and 1.2 times higher than that of pure BiOIO<sub>3</sub> (8.95  $\mu\text{s}$ ) and BiOBr/BiOIO<sub>3</sub> (29.10  $\mu\text{s}$ ), respectively. The above obtained quantitative indexes were generalized in two contrastive schematic diagrams as shown in Fig. 8. Overall, the multiple spectral results uncovered that the dramatically strengthened charge separation and transfer efficiency caused by Sn-doping played significant roles in the photocatalytic performance of Sn-doped BiOBr/BiOIO<sub>3</sub> systems.

In order to further disclose the photogenerated charge migration mechanism and the role of Sn doping for the composite, the electronic structures of the vertical Sn-BiOBr/BiOIO<sub>3</sub> heterostructures were built and analyzed by DFT calculations. The geometric structure of the composite were shown in Fig. S19a. According to the SEM images, the Sn-BiOBr particles were grown on the surface of BiOIO<sub>3</sub>, therefore we

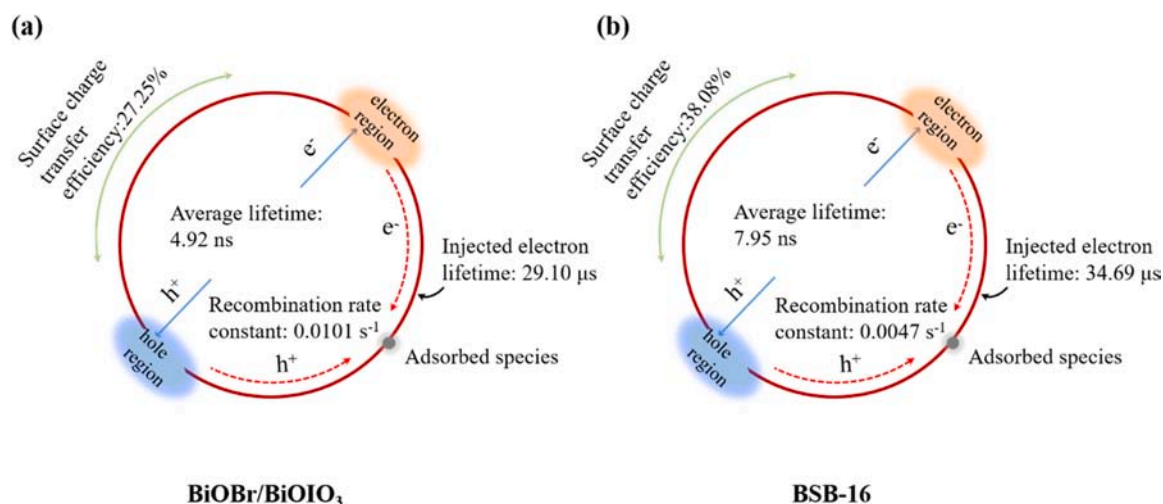


Fig. 8. Schematic illustration of photogenerated charge behaviors: (a) undoped BiOBr/BiOIO<sub>3</sub> composite and (b) BSB-16 composite.

chose a vertical arrangement rather than parallel in-plane model (Fig. S19b). The Br-terminated Sn-BiOBr (001) and IO<sub>3</sub>-terminated BiOIO<sub>3</sub> were chosen to construct the hybrid layered nanocomposite because halogen-terminated bulk had been confirmed to possess much higher thermodynamic stability than BiO-terminated one [50]. A 2 × 2 unit cell of Sn-BiOBr was a rectangular cell of 7.84 Å × 7.84 Å, which could match with a  $\sqrt{2} \times \sqrt{2}$  unit cell of BiOIO<sub>3</sub> with a 2D rectangular cell of 8.07 Å × 8.07 Å. The mismatch of lattice was only 2.9% (far less than 5%), giving rise to minor compressed deformation of BiOIO<sub>3</sub>. The optimized vertical interface spacing was ca. 2.9 Å, closing with the previously reported interlayer distance of BiOI/BiOIO<sub>3</sub> (3.0 Å) [51]. Furthermore, the vertical BiOBr/BiOIO<sub>3</sub> structure was also constructed as comparison (Fig. S19c). For evaluating the relative stability, the binding energy of the hetero-structure models was calculated according to the following definition [52]:

$$\Delta E(\text{Sn} - \text{BiOBr}/\text{BiOIO}_3) = E(\text{Sn} - \text{BiOBr}/\text{BiOIO}_3) - E(\text{Sn} - \text{BiOBr}) - E(\text{BiOIO}_3) \quad (4)$$

$$\Delta E(\text{BiOBr}/\text{BiOIO}_3) = E(\text{BiOBr}/\text{BiOIO}_3) - E(\text{BiOBr}) - E(\text{BiOIO}_3) \quad (5)$$

where  $E(\text{Sn} - \text{BiOBr}/\text{BiOIO}_3)$  and  $E(\text{BiOBr}/\text{BiOIO}_3)$  were the total energies of the heterostructures,  $E(\text{Sn} - \text{BiOBr})$ ,  $E(\text{BiOBr})$  and  $E(\text{BiOIO}_3)$  represented the total energies of Sn-BiOBr slab, BiOBr slab and the BiOIO<sub>3</sub> slab, respectively. The calculated binding energies of Sn-BiOBr/BiOIO<sub>3</sub> and BiOBr/BiOIO<sub>3</sub> were calculated to be -1.79 eV and -1.76 eV, respectively. All the interface energies were negative and the Sn-BiOBr/BiOIO<sub>3</sub> with lower binding energy was relatively steadier than BiOBr/BiOIO<sub>3</sub> heterostructure. These results indicated that Sn-doping could enhance the stability of heterojunction, which provided a precondition for the formation of directional charge transfer channel.

Based on the geometrically optimized Sn-BiOBr/BiOIO<sub>3</sub> model, the electronic properties were surveyed. Fig. 9a showed the TDOS and PDOS. The Fermi level was set at 0 eV. Obviously, the band gap of composite was mostly narrowed compared with Sn-BiOBr and BiOIO<sub>3</sub>, making it easier to get excited electrons from VB to the CB under light irradiation. Moreover, one could also see that the DOS of Sn-BiOBr/BiOIO<sub>3</sub> crossed the Fermi level, indicating that the heterojunction possessed semi-metallic characteristic. In order to uncover the origin of the semi-metallic characteristic, the TDOS and PDOS of undoped BiOBr/BiOIO<sub>3</sub> was also calculated as shown in Fig. S20. The VBM was located near the Fermi level which had no semi-metallic characteristic [53]. Thus, Sn-doping was inferred to result in the appearance of semi-metallic characteristic in Sn-BiOBr/BiOIO<sub>3</sub>. In other words, Sn-BiOBr/BiOIO<sub>3</sub> exhibited higher hole concentration at the VB edge in

comparison with the undoped composite, which inferred the higher transition probability of photoinduced electrons to the CB under light illumination [54]. PDOS images illustrated that the CBM was primarily occupied by Bi p-orbital, O p-orbital and I p-orbital, while except O p-orbital and Br p-orbital, Sn s-orbital and p-orbital also participated in it. Whereas, unlike BiOBr/BiOIO<sub>3</sub>, the asymmetrical spin-up and spin-down states around the Fermi level of Sn-BiOBr/BiOIO<sub>3</sub> suggested a spin-polarized effect caused by the substitution of Bi atom with Sn atom [55]. The obvious electron polarization that can provide more spin-down photoinduced electrons under light irradiation. The 3D visualized band charge density distribution of Sn-BiOBr/BiOIO<sub>3</sub> composite was further calculated to investigate the migration of photo-generated carriers. As displayed in Fig. 9b and c, the HOMO was composed by Sn-BiOBr, whereas the LUMO was occupied by BiOIO<sub>3</sub>, consistent with the results of DOS. When the Sn-BiOBr/BiOIO<sub>3</sub> composite exposed to the light, the photoexcited electrons at Sn-BiOBr could easily transport to BiOIO<sub>3</sub>, and left behind the photogenerated holes at Sn-BiOBr. Consequently, the photogenerated carriers would be segregated spatially, benefiting to the catalytic performance of the composite.

Since the Sn-doping imposed significant impact on the electronic properties of Bi-BiOBr/BiOIO<sub>3</sub> composites, for purpose of understanding the relationship of the accelerated charge separation at the interface and the introduction of Sn, 3D charge density difference and planar averaged differential charge density were theoretically determined. As shown in Fig. 9d and e, the yellow and blue colors denoted the electron accumulation and depletion, respectively. It could be clearly seen that the charge transfer mainly occurred between the I atoms of BiOIO<sub>3</sub> and the Br atoms of Sn-BiOBr at the interface. It was worth noting that the Sn atom tended to slightly accept electrons after forming heterojunction, which was counter to that in single Sn-BiOBr. This implied that Sn dopant would also tune the electric field in Sn-BiOBr/BiOIO<sub>3</sub> composite and it might act as an electron donor near the VB. The planar averaged differential charge density offered a quantitative base for analysing the interfacial charge redistribution, which was defined as:

$$\Delta\rho = \rho(\text{Sn} - \text{BiOBr}/\text{BiOIO}_3) - \rho(\text{Sn} - \text{BiOBr}) - \rho(\text{BiOIO}_3) \quad (6)$$

where  $\rho(\text{Sn} - \text{BiOBr}/\text{BiOIO}_3)$ ,  $\rho(\text{Sn} - \text{BiOBr})$  and  $\rho(\text{BiOIO}_3)$  were the charge densities of heterojunction and isolated component, respectively. It could be realized that the electrons primarily accumulated at Sn-BiOBr and a distinct electron delocalization happened on IO<sub>3</sub> pyramids. The charge redistribution indicated the formation of a strong built-in electric field at the Sn-BiOBr/BiOIO<sub>3</sub> interface with dominant direction from BiOIO<sub>3</sub> to Sn-BiOBr. Thus, the photoexcited electrons could transfer across the interface readily. Considering the matched band structures of

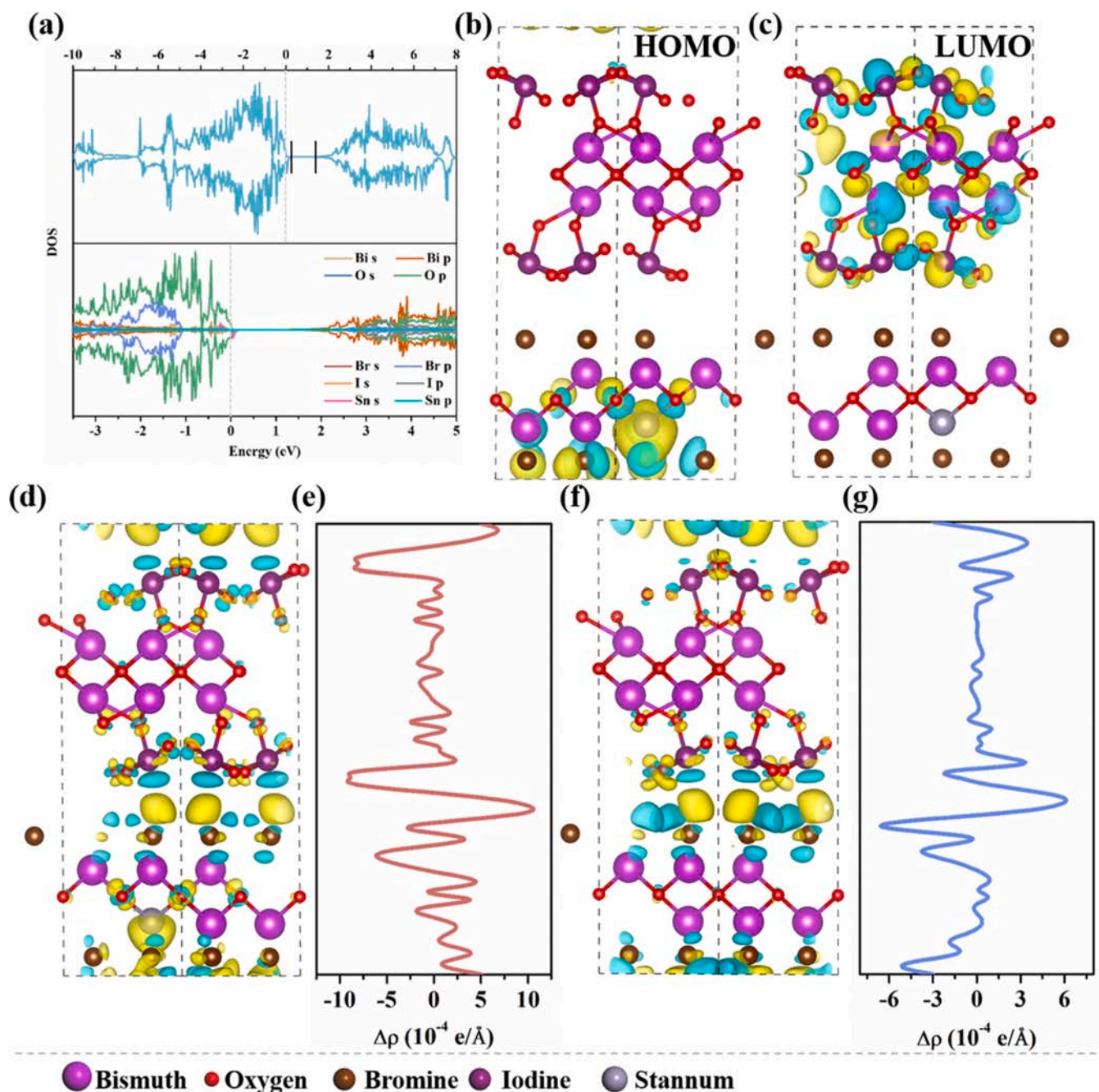


**Fig. 9.** (a) The total density of states (TDOS) and partial density of states (PDOS) of the Sn-BiOBr/BiOIO<sub>3</sub> model. (b) The highest occupied molecular orbital (HOMO) and (c) the lowest unoccupied molecular orbital (LUMO) of Sn-BiOBr/BiOIO<sub>3</sub>. (d) 3D charge density difference and (e) the corresponding planar averaged charge density difference for Sn-doped BiOBr/BiOIO<sub>3</sub>. (f) 3D charge density difference and (g) the corresponding planar averaged charge density difference for undoped BiOBr/BiOIO<sub>3</sub>.

pure BiOBr with BiOIO<sub>3</sub>, the charge density difference at the interface of undoped BiOBr/BiOIO<sub>3</sub> composite was also investigated as shown in Fig. 9f and g. Intuitively, apart from the electron migration from Br atoms to I atoms, another electronic channel from O atoms in IO<sub>3</sub> pyramids to Br atoms was also existed. This made the charge exchange relatively disordered than that in Sn-BiOBr/BiOIO<sub>3</sub>. The corresponding planar differential charge density showed that much less electrons were transferred between the interface of undoped BiOBr and BiOIO<sub>3</sub>, which indicated a reduction of driving force at the interface. The DFT simulated results strongly validated that the doping of Sn was conducive to the magnification of interfacial electric field and Sn atom had electronic elasticity to function as electron donor and acceptor simultaneously.

Therefore, the interfacial charge transfer was greatly promoted.

### 3.6. Photocatalytic mechanism

In light of the above measurements and simulation, a tentative photocatalytic mechanism of Sn-BiOBr/BiOIO<sub>3</sub> heterojunction for pollutant removal and CO<sub>2</sub> reduction was proposed as shown in Fig. 10. Under visible or simulated solar light irradiation, both Sn-BiOBr and BiOIO<sub>3</sub> could be excited. Due to the Sn<sup>2+</sup>/Sn<sup>4+</sup> redox couple between the CB and VB of Sn-BiOBr, the electrons could easily transfer to the CB via the springboard, validly retarding the recombination of photo-generated charge carriers. This gave a possibility that more charges

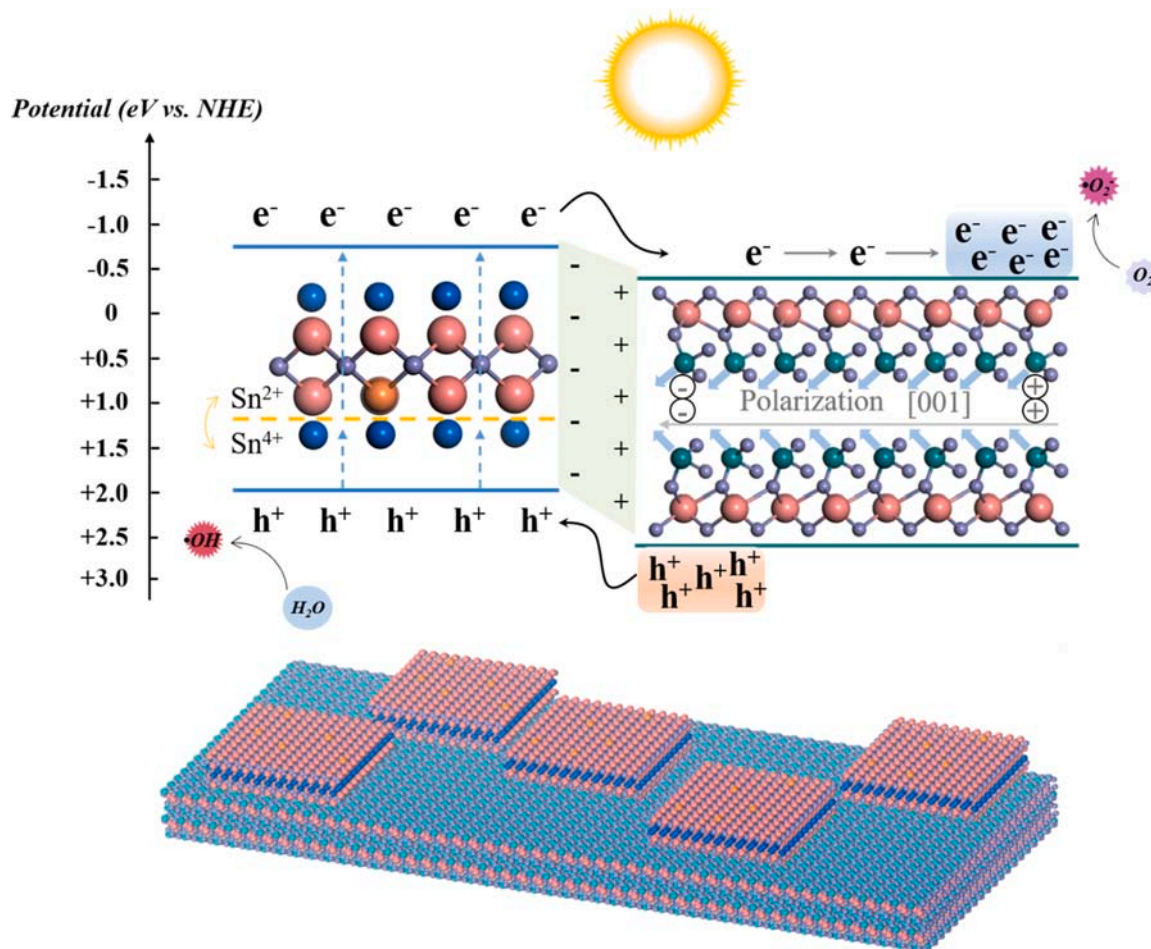


Fig. 10. Schematic illustration of photocatalytic mechanism for Sn-BiOBr/BiOIO<sub>3</sub> composite under light irradiation.

could participate in the subsequent processes. In terms of the above results, the CB position and VB position of Sn-BiOBr and BiOIO<sub>3</sub> were  $-0.78$  eV,  $-0.44$  eV and  $+2.00$  eV,  $+2.57$  eV, respectively. The stagger arrangement thermodynamically impelled the electrons to migrate from Sn-BiOBr to BiOIO<sub>3</sub> and holes transfer along an opposite direction. Because of the electronic modulation by Sn doping, a large interfacial electric field was generated at the interface with an orientation from BiOIO<sub>3</sub> to Sn-BiOBr. Therefore, the charge transfer became significantly ordered and rapid. It was well-known that BiOIO<sub>3</sub> owned a powerful electric field along c-axis caused by the asymmetrical distribution of IO<sub>3</sub> pyramids with uneven charge distribution in space. When the photoinduced electrons arrived at BiOIO<sub>3</sub>, the internal polar field would drive them to migrate swiftly and accumulate at the (001) facet. Finally, the photogenerated charges realized effective spatial separation with a prolonged lifetime to reduce and oxidize the relevant reactants.

#### 4. Conclusion

In summary, *in situ* growth of Sn-doped BiOBr on the surface of BiOIO<sub>3</sub> was successfully achieved *via* a simply partial etching approach. The obtained Sn-BiOBr/BiOIO<sub>3</sub> samples owned improved optical absorption and charge migration properties, which exhibited excellence performance for organic pollutants degradation and CO<sub>2</sub> photoreduction. Experimental data and DFT calculation results indicated that the Sn-doping tactfully modulated the electron distribution, enlarging the built-in electric fields at the interface. The photocatalyst exhibited superior catalytic activities upon the degradation of TC, 2, 4-DCP and RhB, and reached 85.66 %, 80.01 % and 99.90 % within 60 min or 20 min, respectively. Also, the photocatalytic reduction efficiency of CO<sub>2</sub> was

improved to  $7.40 \mu\text{mol g}^{-1} \text{h}^{-1}$ . This study exposed the promising prospect of modulated interfacial electric field *via* impurity doping, and might have potentials to be applied to other bismuth-based semiconductors.

#### CRediT authorship contribution statement

**Hanbo Yu:** Conceptualization, Methodology, Software, Investigation, Writing - original draft. **Jinhui Huang:** Conceptualization, Resources, Project administration, Funding acquisition. **Longbo Jiang:** Data curation. **Lijian Leng:** Validation. **Kaixin Yi:** Formal analysis. **Wei Zhang:** Investigation. **Chenyu Zhang:** Validation. **Xingzhong Yuan:** Supervision, Funding acquisition.

#### Declaration of Competing Interest

The authors declare that they have no known competing financial interests or personal relationships that could have appeared to influence the work reported in this paper.

#### Acknowledgement

This study was financially supported by the National Natural Science Foundation of China (51739004, 51578222 and 51521006).

#### Appendix A. Supplementary data

Supplementary material related to this article can be found, in the online version, at doi:<https://doi.org/10.1016/j.apcatb.2021.120618>.

## References

- [1] Y. Pan, X. Yuan, L. Jiang, H. Wang, H. Yu, J. Zhang, *Chem. Eng. J.* 384 (2020), 123310.
- [2] X. Zhang, X. Yuan, L. Jiang, J. Zhang, H. Yu, H. Wang, G. Zeng, *Chem. Eng. J.* 390 (2020), 124475.
- [3] J. Liu, Y. Liu, N. Liu, Y. Han, X. Zhang, H. Huang, Y. Lifshitz, S.T. Lee, J. Zhong, Z. Kang, *Science* 347 (2015) 970–974.
- [4] R. Asahi, T. Morikawa, T. Ohwaki, K. Aoki, Y. Taga, *Science* 293 (2001) 269–271.
- [5] Y. Shi, J. Huang, G. Zeng, W. Cheng, H. Yu, Y. Gu, L. Shi, K. Yi, *J. Colloid Interface Sci.* 531 (2018) 433–443.
- [6] J. Huang, J. Hu, Y. Shi, G. Zeng, W. Cheng, H. Yu, Y. Gu, L. Shi, K. Yi, *J. Colloid Interface Sci.* 541 (2019) 356–366.
- [7] Y. Shi, J. Huang, G. Zeng, W. Cheng, J. Hu, L. Shi, K. Yi, *Chemosphere* 230 (2019) 40–50.
- [8] S. Zhang, Z. Liu, W. Yan, Z. Guo, M. Ruan, *Chinese J. Catal.* 41 (2020) 1884–1893.
- [9] H. Yu, J. Huang, L. Jiang, X. Yuan, K. Yi, W. Zhang, J. Zhang, H. Chen, *Chem. Eng. J.* (2020), 127334.
- [10] H. Wang, H. Wang, Z. Wang, L. Tang, G. Zeng, P. Xu, M. Chen, T. Xiong, C. Zhou, X. Li, D. Huang, Y. Zhu, Z. Wang, J. Tang, *Chem. Soc. Rev.* 49 (2020) 4135–4165.
- [11] H. Li, S. Sun, H. Ji, W. Liu, Z. Shen, *Appl. Catal. B* 272 (2020), 118966.
- [12] L. Jiao, G. Wan, R. Zhang, H. Zhou, S.H. Yu, H.L. Jiang, *Angew. Chemie* 57 (2018) 8525–8529.
- [13] G. Fang, Z. Liu, C. Han, *Appl. Surf. Sci.* 515 (2020), 146095.
- [14] S. Zhang, Z. Liu, D. Chen, Z. Guo, M. Ruan, *Chem. Eng. J.* 395 (2020), 125101.
- [15] G. Yao, S. Yang, J. He, S. Jiang, C. Sun, S. Song, *Appl. Catal. B* 287 (2021), 119986.
- [16] C. Feng, L. Tang, Y. Deng, J. Wang, W. Tang, Y. Liu, Z. Chen, J. Yu, J. Wang, Q. Liang, *Chem. Eng. J.* 389 (2020), 124474.
- [17] Y. Wang, J. Jin, W. Chu, D. Cahen, T. He, *ACS Appl. Mater. Interfaces* 10 (2018) 15304–15313.
- [18] W. Shi, J. Shi, S. Yu, P. Liu, *Appl. Catal. B* 138–139 (2013) 184–190.
- [19] Z. Xing, J. Hu, M. Ma, H. Lin, Y. An, Z. Liu, Y. Zhang, J. Li, S. Yang, *J. Am. Chem. Soc.* 141 (2019) 19715–19727.
- [20] H. Yu, L. Jiang, H. Wang, B. Huang, X. Yuan, J. Huang, J. Zhang, G. Zeng, *Small* 15 (2019), e1901008.
- [21] L. Jiang, X. Yuan, G. Zeng, J. Liang, Z. Wu, H. Yu, D. Mo, H. Wang, Z. Xiao, C. Zhou, *J. Colloid Interface Sci.* 536 (2019) 17–29.
- [22] J. Guo, X. Liao, M. Lee, G. Hyett, C. Huang, D.W. Hewak, S. Mailis, W. Zhou, Z. Jiang, *Appl. Catal. B* 243 (2019) 502–512.
- [23] H. Ji, L. Lyu, L. Zhang, X. An, C. Hu, *Appl. Catal. B* 199 (2016) 230–240.
- [24] J. Cao, X. Li, H. Lin, S. Chen, X. Fu, *J. Hazard. Mater.* 239–240 (2012) 316–324.
- [25] H. Deng, F.J. Lamelas, J.M. Hosselopp, *Chem. Mater.* 15 (2003) 2429–2436.
- [26] X. Zhang, D. Wang, X. Man, J. Wu, Q. Liu, Y. Qi, Z. Liu, X. Zhao, J. Wu, C. Hao, *J. Colloid Interface Sci.* 558 (2020) 123–136.
- [27] L. Xu, W. Chen, S. Ke, M. Zhu, W. Qiu, N. Liu, S. Namuanguk, P. Maitarak, S. Impeng, L. Tang, *Catal. Sci. Technol.* 9 (2019) 5953–5961.
- [28] X. Tu, S. Qian, L. Chen, L. Qu, *J. Mater. Sci.* 50 (2015) 4312–4323.
- [29] J. Wan, J. Huang, H. Yu, L. Liu, Y. Shi, C. Liu, *J. Colloid Interface Sci.* 601 (2021) 229–241.
- [30] H. Huang, S. Tu, C. Zeng, T. Zhang, A.H. Reshak, Y. Zhang, *Angew. Chemie* 56 (2017) 11860–11864.
- [31] J. Di, M. Ji, J. Xia, X. Li, W. Fan, Q. Zhang, H. Li, *J. Mol. Catal. A Chem.* 424 (2016) 331–341.
- [32] W. Wang, Q. Niu, G. Zeng, C. Zhang, D. Huang, B. Shao, C. Zhou, Y. Yang, Y. Liu, H. Guo, W. Xiong, L. Lei, S. Liu, H. Yi, S. Chen, X. Tang, *Appl. Catal. B* 273 (2020), 119051.
- [33] Y. Huo, J. Zhang, M. Miao, Y. Jin, *Appl. Catal. B* 111–112 (2012) 334–341.
- [34] F.R. Sensato, R. Custodio, E. Longo, A. Beltrán, J. Andrés, *Catal. Today* 85 (2003) 145–152.
- [35] V.B.R. Boppa, R.F. Lobo, *J. Catal.* 281 (2011) 156–168.
- [36] Y. Yang, G. Zeng, D. Huang, C. Zhang, D. He, C. Zhou, W. Wang, W. Xiong, X. Li, B. Li, W. Dong, Y. Zhou, *Appl. Catal. B* 272 (2020), 118970.
- [37] L. Liu, J. Huang, H. Yu, J. Wan, L. Liu, K. Yi, W. Zhang, C. Zhang, *Chemosphere* 282 (2021), 131049.
- [38] C. Li, Y. Ma, S. Zheng, C. Hu, F. Qin, L. Wei, C. Zhang, S. Duo, Q. Hu, *J. Colloid Interface Sci.* 576 (2020) 291–301.
- [39] F. Chen, H. Huang, L. Ye, T. Zhang, Y. Zhang, X. Han, T. Ma, *Adv. Funct. Mater.* 28 (2018), 1804284.
- [40] S. Li, L. Bai, N. Ji, S. Yu, S. Lin, N. Tian, H. Huang, *J. Mater. Chem. A* 8 (2020) 9268–9277.
- [41] L. Hao, L. Kang, H. Huang, L. Ye, K. Han, S. Yang, H. Yu, M. Batmunkh, Y. Zhang, T. Ma, *Adv. Mater.* 31 (2019), e1900546.
- [42] H. Wang, D. Jiang, D. Huang, G. Zeng, P. Xu, C. Lai, M. Chen, M. Cheng, C. Zhang, Z. Wang, *J. Mater. Chem. A* 7 (2019) 22848–22870.
- [43] L. Liu, H. Huang, Z. Chen, H. Yu, K. Wang, J. Huang, H. Yu, Y. Zhang, *Angew. Chemie* (2021).
- [44] Y. Hou, T. Li, S. Yan, Z. Zou, *Appl. Catal. B* 269 (2020), 118777.
- [45] D. Monllor-Satoca, R. Gomez, W. Choi, *Environ. Sci. Technol.* 46 (2012) 5519–5527.
- [46] A. Zaban, M. Greenshtein, J. Bisquert, *Chemphyschem* 4 (2003) 859–864.
- [47] J. Bisquert, V.S. Vikhrenko, *J. Phys. Chem. B* 108 (2004) 2313–2322.
- [48] D. Monllor-Satoca, R. Gómez, *J. Phys. Chem. C* 112 (2007) 139–147.
- [49] S. Sun, W. Wang, L. Zhang, *J. Phys. Chem. C* 117 (2013) 9113–9120.
- [50] H. Zhang, L. Liu, Z. Zhou, *RSC Adv.* 2 (2012) 9224.
- [51] W. Dai, Z. Zhao, *Phys. Chem. Chem. Phys.* 19 (2017) 9900–9911.
- [52] B. Gao, J. Zhang, L. Chen, J. Guo, S. Shen, C. Au, S. Yin, M. Cai, *Appl. Surf. Sci.* 492 (2019) 157–165.
- [53] J. Li, X. Wu, W. Pan, G. Zhang, H. Chen, *Angew. Chemie* 57 (2018) 491–495.
- [54] S. Gao, B. Gu, X. Jiao, Y. Sun, X. Zu, F. Yang, W. Zhu, C. Wang, Z. Feng, B. Ye, Y. Xie, *J. Am. Chem. Soc.* 139 (2017) 3438–3445.
- [55] G. Jiang, X. Wang, Z. Wei, X. Li, X. Xi, R. Hu, B. Tang, R. Wang, S. Wang, T. Wang, W. Chen, *J. Mater. Chem. A* 1 (2013) 2406.